AGU PUBLICATIONS

JGR

Journal of Geophysical Research: Space Physics

RESEARCH ARTICLE
10.1002/2014JA020060

Key Points:
- Mantle appearance is dawn-dusk asymmetric depending on IMF By direction
- Low-latitude mantle plasma mainly comes from the magnetopause source
- Magnetopause source for mantle moves to lower latitudes when IMF By is dominant

Correspondence to:
C.-P. Wang,
cat@atmos.ucla.edu

Citation:
Wang, C.-P., L. R. Lyons, and V. Angelopoulos (2014), Properties of low-latitude mantle plasma in the Earth's magnetotail: ARTEMIS observations and global MHD predictions, *J. Geophys. Res. Space Physics*, *119*, doi:10.1002/2014JA020060.

Received 7 APR 2014
Accepted 25 AUG 2014
Accepted article online 27 AUG 2014

Properties of low-latitude mantle plasma in the Earth's magnetotail: ARTEMIS observations and global MHD predictions

Chih-Ping Wang[1], Larry R. Lyons[1], and Vassilis Angelopoulos[2]

[1]Department of Atmospheric and Oceanic Sciences, University of California, Los Angeles, California, USA, [2]Institute of Geophysics and Planetary Physics, University of California, Los Angeles, California, USA

Abstract The Earth's plasma mantle is one of the major suppliers of particles for the plasma sheet. To understand its plasma characteristics, spatial distributions, and dependencies on interplanetary magnetic field (IMF) direction, we statistically analyzed the Acceleration, Reconnection, Turbulence, and Electrodynamics of Moon's Interaction with the Sun (ARTEMIS) observations in the low-latitude magnetotail (~10 R_E above and below the current sheet) and investigated the predictions from global Block Adaptive Tree Solar wind-Roe-Upwind Scheme MHD simulations. The mantle plasma flows tailward along magnetic field lines (~50–200 km/s) and at the same time drifts toward midnight and toward the current sheet. The mantle plasma has similar temperature (~0.05–0.2 keV) to the magnetosheath plasma but has lower density (~0.1–1 cm^{-3}). The mantle appearance is dawn-dusk asymmetric depending mainly on the IMF B_y direction. The occurrence rates, density, and $V_{||}$ all decrease with decreasing $|Y|$. This density cross-tail profile suggests that the low-latitude mantle plasma mainly comes from the magnetosheath entering through the tail magnetopause along the open field lines. Density is highly and positively correlated with $V_{||}$. These observations are qualitatively consistent with the MHD results. The simulations indicate that as IMF B_y becomes dominant, the source locations at the magnetopause for the mantle move to lower latitudes and become dawn-dusk asymmetric, and the tail cross section also becomes distorted with the magnetopause shape elongating and the current sheet tilting significantly. Degrees of these changes also vary with the downtail distances and IMF B_z direction. The source location change leads to the dawn-dusk asymmetric mantle appearance. The tail cross-section change alters the distance from the sources to the current sheet and thus the resulting mantle density distributions just outside the plasma sheet.

1. Introduction

The mantle plasma [e.g., *Hones et al.*, 1972; *Rosenbauer et al.*, 1975] is magnetosheath-like plasma in the magnetosphere flowing tailward along the open magnetic field lines but with reduced density and tailward speed than the magnetosheath. It also $E \times B$ drifts toward the current sheet, and its subsequent entry into the closed field line region of the magnetotail makes it one of the major suppliers of particles for the plasma sheet. The mantle plasma consists of particles originating in the cusp (referred to as the cusp source hereafter) and particles entering through the magnetotail magnetopause along open field lines (referred to as the magnetopause source hereafter) [*Siscoe and Sanchez*, 1987; *Siscoe et al.*, 2001]. (Note that plasma from the ionosphere can mix with plasma from the cusp source [e.g., *Candidi et al.*, 1982].) The locations and strengths (density) of these two sources, together with the parallel and perpendicular velocities of the mantle particles, determine the spatial distribution of mantle plasma in the magnetotail and thus the amount of particles it supplies into the plasma sheet [*Pilipp and Morfill*, 1978]. However, current understanding of the characteristics and spatial distributions of the mantle plasma and their dependencies on the interplanetary magnetic field (IMF) conditions provided by past observations and models/simulations has been quite limited.

Past observations focused mostly on where the mantle plasma appears. It can appear in the near-Earth region [e.g., *Haerendel and Paschmann*, 1975; *Taguchi et al.*, 2001], at the lunar distances [e.g., *Hardy et al.*, 1975, 1976, 1979], and in the distant tail [e.g., *Gosling et al.*, 1984; *Maezawa and Hori*, 1998; *Seki et al.*, 1998]. Across the tail, it can be seen at either high or low latitudes [e.g., *Siscoe and Kaymaz*, 1999], and its appearance on the dawn or dusk sides is strongly controlled by the IMF B_y direction. On the other hand, little is known on how the plasma parameters and fields associated with the mantle plasma vary spatially [e.g., *Akinrimisi et al.*, 1990] due to the limited spatial coverage of the data used in the past

studies. Now sufficient measurements provided by the Acceleration, Reconnection, Turbulence, and Electrodynamics of Moon's Interaction with the Sun (ARTEMIS) mission allow us to determine the spatial distributions of the mantle plasma in the magnetotail.

Past models/simulations have revealed many important factors, including sources and velocities, crucial to the mantle spatial distributions [*Pilipp and Morfill*, 1978; *Grzedzielski and Macek*, 1988; *Onsager et al*., 1993; *Richard et al*., 1995; *Siscoe et al*., 2001]. However, the assumptions or simulation conditions used in these studies are rather idealized, and how these factors in the magnetotail change with the solar wind and IMF conditions remains undetermined. Thus, we investigated these factors using the global MHD simulation results provided by the NASA Community Coordinated Modeling Center (CCMC).

In this study, we analyzed the ARTEMIS observations and the Block Adaptive Tree Solar wind-Roe-Upwind Scheme (BATS-R-US) global MHD simulation results to investigate the plasma and field parameters associated with the mantle plasma (ions only) in the low-latitude magnetotail from -40 to -80 R_E and their dependencies on the IMF B_y and IMF B_z directions. In section 2, we describe the ARTEMIS data and the selection of the mantle plasma. We present in section 3 the statistical results of the observed characteristics and cross-tail profiles of the mantle plasma. In section 4, we describe the MHD predictions of the mantle plasma corresponding to different IMF directions. Discussion on how the IMF directions alter the mantle distributions as indicated by the simulations and on some important characteristics of the mantle plasma indicated by the observations are presented in section 5.

2. ARTEMIS Data Processing and Selection

In this study we used the ion and magnetic field measurements from the two ARTEMIS probes (ARTEMIS-B and ARTEMIS-C) [*Sibeck et al*., 2011]. The ARTEMIS probes were originally part of the five Time History of Events and Macroscale Interactions during Substorms (THEMIS) spacecraft in the near-Earth magnetosphere. They started to move outward gradually in early 2010 to their final orbits at the lunar distances (r ~60 R_E). We used the data from August 2010 to December 2012, during which the two probes surveyed the low-latitude magnetotail near the current sheet from $X \sim -40$ to -80 R_E (the spacecraft spent ~4 to 5 days a month in the tail magnetosphere).

The ions are measured by an electrostatic analyzer (ESA, 0.006–20 keV/q [*McFadden et al*., 2008]) and a solid state telescope (SST, 35 keV–6 MeV for ions and 30 keV–6 MeV for electrons). For each measured energy spectrum, contamination to ESA and SST is removed. The sunlight contamination to the SST is also removed (defined by a criterion that considers a data point being contaminated if its modified z-score calculated across azimuthal angle is greater than 3.5. The modified z-score is a normalized outlier detection test [*Iglewicz and Hoaglin*, 1993]. For a data point with value x_i, its modified z-score is $0.6745 \cdot (x_i - x_{\text{median}})/\text{median}(|x_i - x_{\text{median}}|)$.). For ions, there is an energy gap (from ~20 to 28 keV) between the highest ESA channel and the lowest SST channel. We filled this gap by linearly interpolating fluxes from the highest ESA energy and the lowest SST energy to the middle energy of the gap. The total plasma temperature is computed from the combined ESA and SST energy spectrum. The magnetic field is measured by the flux gate magnetometer [*Auster et al*., 2008]. GSM coordinates are used for the plasma bulk velocities and magnetic field vectors. The data were originally in different time resolutions (~3–4 s for the plasma onboard-computed moments and reduced data packets and magnetic field and ~1 or 6 min for the full distributions during slow survey) but were interpolated to a 1 min resolution in this study. Finally, 1 min OMNI solar wind and IMF parameters that have been shifted to the Earth's bow shock nose were then tagged to each ARTEMIS data point.

We identified each THEMIS crossing of the magnetopause and sorted each measurement into regions of the magnetosheath and magnetosphere. From our identified magnetopause crossings, we found that the magnetopause locations are more dawn-dusk symmetric in the aberrated geocentric solar ecliptic (AGSE) coordinates (the aberration angle is determined by observed solar wind velocity that has been time shifted to the Earth's bow shock nose) than are their locations in other coordinates (geocentric solar magnetospheric (GSM), aberrated GSM, geocentric solar wind (GSW), and GSE coordinate). Thus, we used the AGSE coordinates for the spacecraft locations in this study (magnetic field and flow velocity vectors are still in GSM).

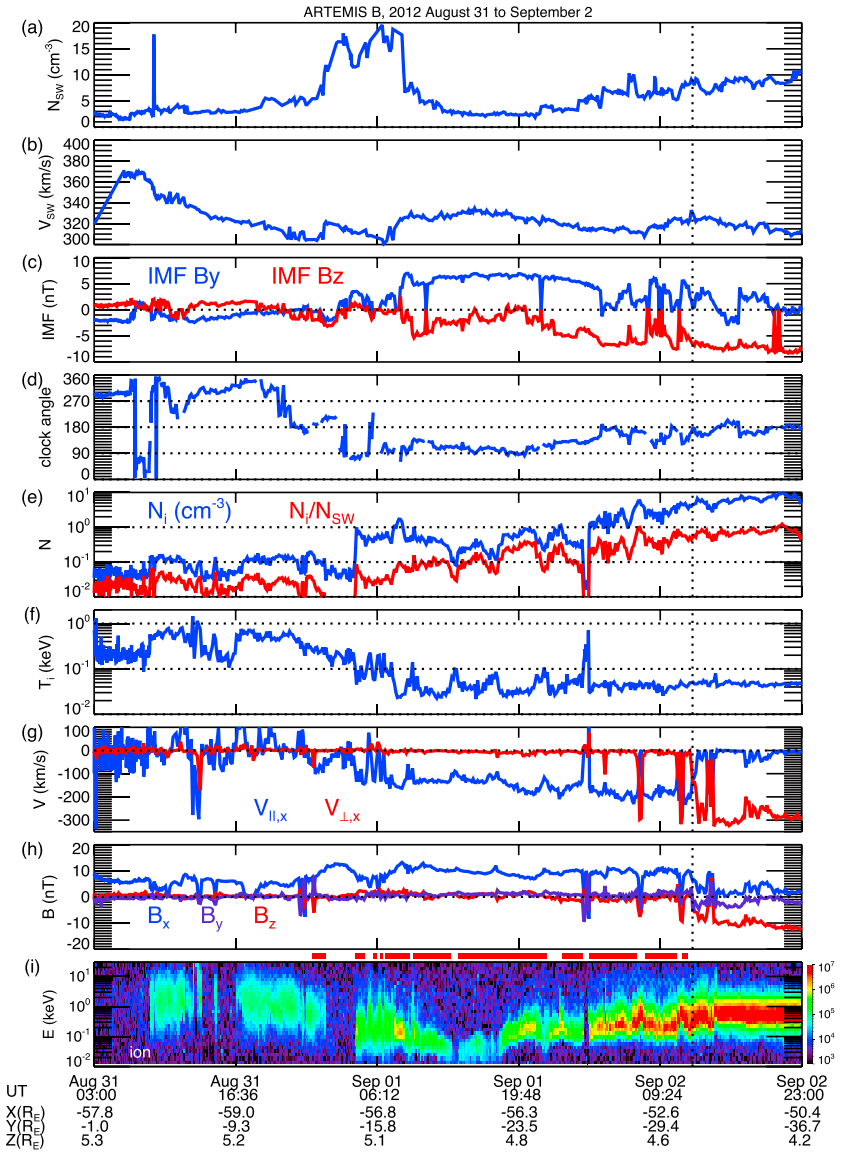

Figure 1. (a) The solar wind density, (b) solar wind speed, (c) IMF B_y and B_z, (d) IMF clock angles from the OMNI data, (e) ion density, (f) ion temperature, (g) ion parallel and perpendicular bulk velocities in the X direction, (h) magnetic field vectors, and (i) energy spectrum of ion energy fluxes (in eV/(s sr cm^2 eV)) observed by ARTEMIS-B from 31 August to 2 September 2012. The red bars above the energy spectrum indicate the mantle plasma. The X, Y, and Z locations are in the AGSE coordinates.

Figure 1 shows an example of the ARTEMIS-B observations as the spacecraft moved from the magnetotail at Y ~0 to the dawnside magnetosheath at $Y \sim -36$ R_E at $X \sim -55$ R_E. ARTEMIS-B crossed the magnetopause at $Y \sim -30$ R_E as indicated by the sharp changes in B_z and $V_{\perp, x}$. B_z was positive inside the magnetopause and immediately became negative in the magnetosheath (the IMF B_z was negative at the time). $V_{\perp, x}$ changed from very small (~10 km/s) inside the magnetosphere to strong tailward flow (~ −300 km/s, similar to the upstream solar wind speed at the time). Inside the magnetosphere, strong (up to ~200 km/s) field-aligned tailward flow can be seen in the region from the magnetopause to $Y \sim -15$ R_E, which we identified as the mantle plasma (marked with the red bars above the energy spectrum plot shown in Figure 1i). Compared with the typical hot ($>$ ~0.7 keV) and tenuous (~0.1 cm^{-3}) plasma sheet plasma seen in $Y \sim -5$ and 12 R_E, the plasma with strong $V_{||}$ has relatively higher density (up to 1 cm^{-3}) and lower temperature ($<$0.1 keV). The density is about an order of magnitude lower than the magnetosheath density while the temperature is similar to the magnetosheath temperature. These plasma characteristics are similar to those of typical high-latitude mantle plasma observed in the near-Earth region [e.g., *Engebretson et al.*, 2012]. During the period when the mantle plasma was observed,

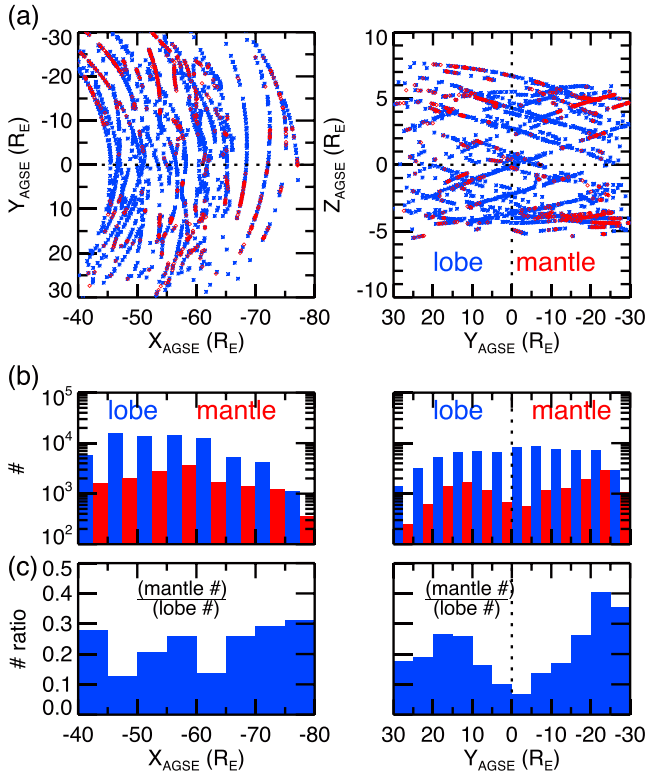

Figure 2. (a) The locations of the two ARTEMIS spacecraft when they were in the lobe region (the blue dots) and when they observed the mantle plasma (the red dots). (b) The number of 1 min data points in the lobe region (blue) and in the mantle (red). (c) The ratios of the number of the mantle data points to that in the lobe region.

the IMF B_y was largely positive (~5 nT), and ARTEMIS-B was in the postmidnight sector above the current sheet ($B_x > \sim 5$ nT) and was away from the current sheet center as indicated by $|B_x| >> |B_z|$. As discussed in section 3.1, these are favorite conditions for the appearance of the mantle plasma. Besides the mantle and plasma sheet plasma, Figure 1 also shows regions (at $Y \sim 0$, -8, and -13 R_E) of very low density ($< \sim 0.07\ cm^{-3}$) where particle fluxes for all energies were extremely low, which we identified as the lobe plasma. Both the mantle plasma and the lobe plasma are in the lobe region, which is loosely defined as the region inside the magnetosphere but outside the plasma sheet (the current sheet). (Note that there could be abundant cold particles from the ionosphere in the lobe region [*André and Cully*, 2012] that cannot be detected unless flowing because their energies are below the ARTEMIS lower energy limit of a few eV.)

As shown in Figure 1, the main characteristics of the mantle plasma (substantial tailward field-aligned flow and sheath-like temperature in the lobe region ($|B_x| >> |B_z|$)) are distinguishably different from those of surrounding hot plasma sheet plasma and very low density lobe plasma, allowing the mantle plasma to be easily separated from the other two by eyes. The mantle plasma is also distinguishably different from the plasma in the low-latitude boundary layer, which consists of < 1 keV cold particles coexisting with hot plasma sheet particles with flow speed much smaller than ~100 km/s. Thus, we first visually examined the plasma moments, magnetic field, and energy spectra to identify the periods of mantle plasma. When the transition from the mantle plasma to the plasma sheet or lobe plasma is very gradual, the separation is somewhat ambiguous. To exclude ambiguous data points, we further selected data within these identified periods with the criteria: $N \geq 0.08\ cm^{-3}$, $N/N_{sw} \leq 1$, $T \leq 0.5$ keV, $|B_x| \geq 5$ nT, and $V_{||,x} \leq -30$ km/s. We also excluded data within 10 R_M to avoid the moon pickup ions, which near the moon surface could have similar temperature and density as the mantle plasma [e.g., *Poppe et al.*, 2012]. Figure 2a shows the *X-Y* and *Y-Z* locations of the ARTEMIS probes when they were in the lobe region (the blue dots) and when they encountered the mantle plasma (the red dots). Since ~99.3% of our mantle plasma has B_z/B_r ($B_r = \sqrt{B_x^2 + B_y^2}$) less than 0.6 and ~98% of it has plasma beta less than 1, we used $B_z/B_r \leq 0.6$ and plasma beta < 1 to identify the ARTEMIS probes being in the lobe region when they were inside the magnetosphere. Thus, the number of the mantle data points is a fraction of the number of the data points in the lobe region. Figure 2b shows the spatial distributions of the numbers of data in the lobe and mantle regions as a function of *X* and *Y*, and Figure 2c shows the ratios of the two numbers that indicate the mantle occurrence rates.

3. ARTEMIS Results

3.1. Occurrence Rates

The occurrence rates over large spatial *X* and *Y* ranges and for all IMF conditions shown in Figure 2 indicate that the mantle plasma can be observed by ARTEMIS throughout the magnetotail with more frequent occurrence at larger $|Y|$ but no preference in *X*. However, when considering the appearance within smaller

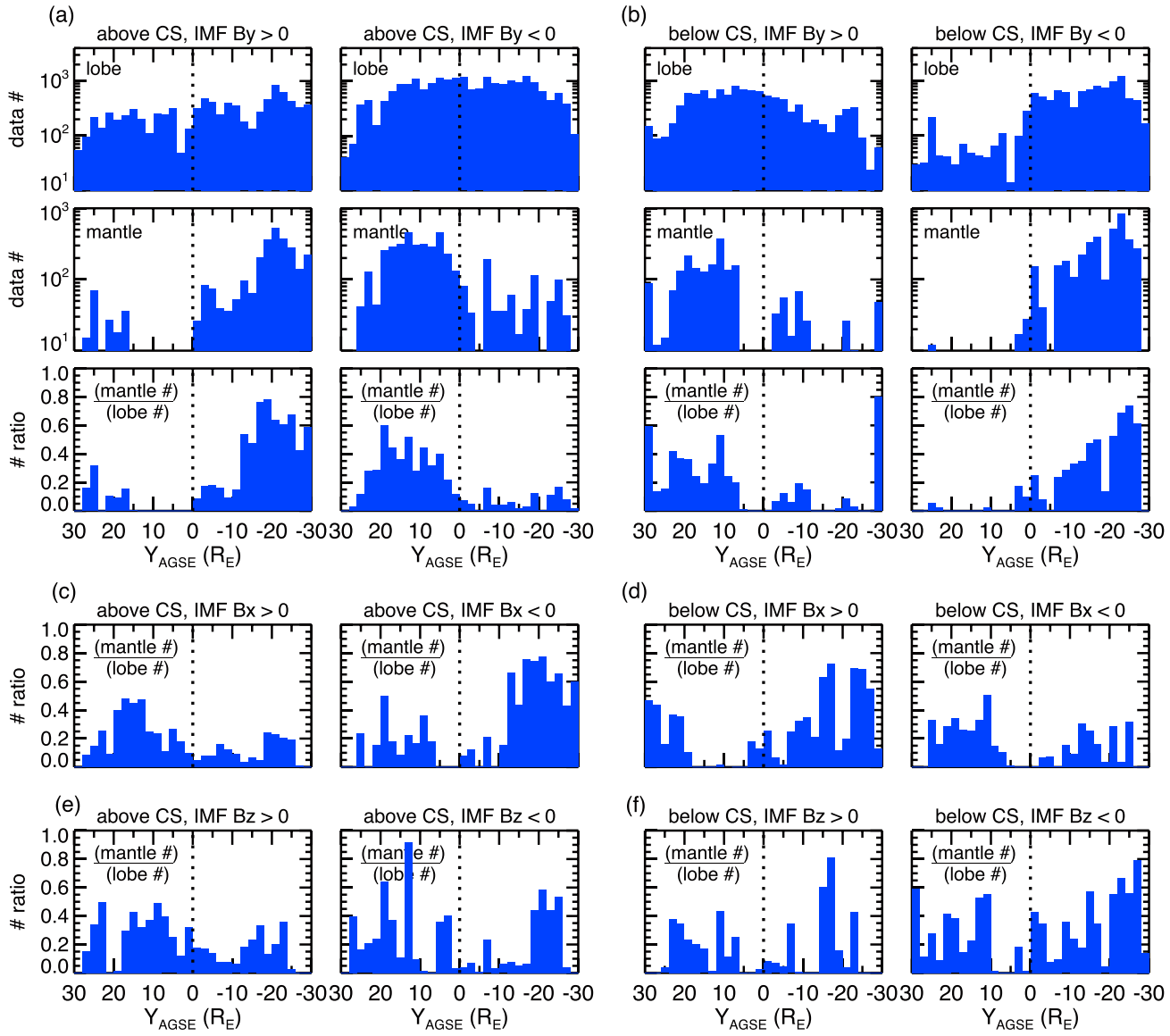

Figure 3. The number of data points in the lobe region and the mantle, the ratios of the number of the mantle data points to that in the lobe region under positive or negative IMF B_y at (a) above and (b) below the current sheet. The ratios of the number of the mantle data points to that in the lobe region under positive or negative IMF B_x at (c) above and (d) below the current sheet. The ratios of the number of the mantle data points to that in the lobe region under positive or negative IMF B_z at (e) above and (f) below the current sheet. The IMF data are 4 h averages.

spatial ranges and its correlations with the IMF parameters, the occurrence rates at different locations are found to depend strongly on the IMF B_y direction. Figure 3 shows the occurrence rate as a function of Y ($-40 < X < -80\ R_E$) in the region above or below the current sheet under different directions of the IMF. Since the mantle plasma observed at smaller $|Y|$ entered the magnetosphere earlier and drifted across the magnetotail to that Y location, the mantle plasma moments near midnight correspond to longer IMF history than do those observed near the flanks. Thus, we averaged the IMF over the period of 4 h prior to the time of the ARTEMIS measurement to take into account the history of IMF. Four hours is roughly the upper limit of the timescale for the mantle plasma to move 20 R_E (half of the tail width) with 10 km/s drift speed. The mantle plasma above the current sheet ($B_x > 0$) appears dominantly in the postmidnight (premidnight) sector when the IMF B_y is positive (negative). The opposite dawn-dusk asymmetry is found for the appearance of the mantle plasma in the region below the current sheet ($B_x < 0$). This is consistent with the findings of *Hardy et al.* [1976] at the lunar distances. The occurrence rates can be > 50% near the flanks but decrease quickly with decreasing $|Y|$ to nearly 0% at midnight. On the other hand, Figures 3c and 3d show that there are

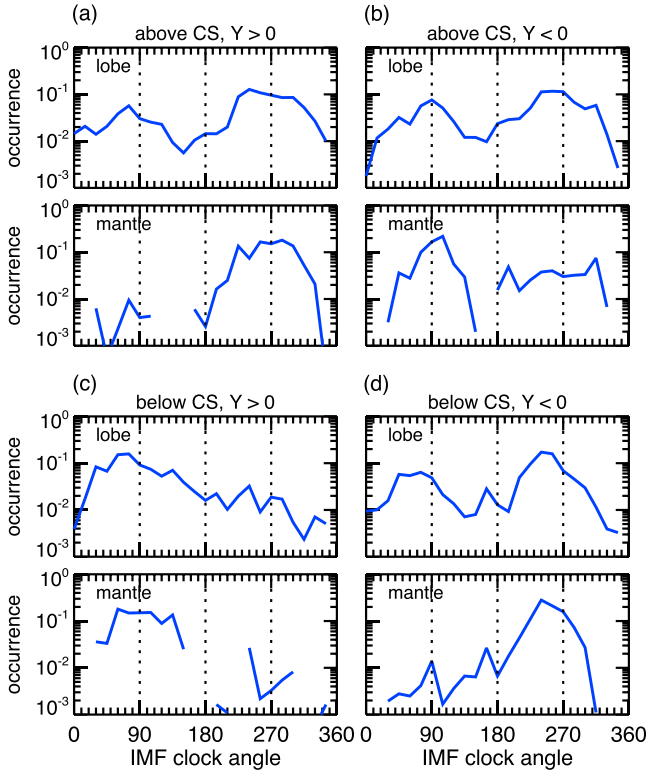

Figure 4. The probabilities of IMF clock angles for the lobe data and mantle data points at above the current sheet and at (a) $Y > 0$ and (b) $Y < 0$ and for data points at below the current sheet and at (c) $Y > 0$ and (d) $Y < 0$. The IMF data are 4 h averages.

no clear dawn-dusk asymmetries corresponding to the directions of IMF B_x or IMF B_z. Note that we have also investigated the Y distributions of the occurrence rate using the IMF averaged over the period of 1 h. The dawn-dusk asymmetries and their dependence on the 1 h averaged IMF directions are essentially the same as the above results. *Hardy et al.* [1979] attributed the dawn-dusk asymmetries to dawn-dusk asymmetric convection speed resulting from nonzero IMF B_y. In sections 4 and 5, we will discuss, together with the MHD results, the factors contributing to the dawn-dusk asymmetries due to the IMF B_y.

Hardy et al. [1979] reported that the mantle plasma at the lunar distances was observed more frequently during *S* IMF than *N* IMF. As can be seen in Figures 3d and 3f, the ARTEMIS results at some Y locations show higher occurrence peaks during *S* IMF than *N* IMF. However, these IMF B_z dependencies may be biased by the occurrence of IMF B_y. Figure 4 shows the probability distributions of the IMF clock angle (θ_{IMF}) for all the lobe data and for the mantle data (θ_{IMF} is the angle between the IMF B_y and IMF B_z: 0° is when IMF $B_y = 0$ and IMF B_z is positive; 90° is when IMF B_y is positive and IMF $B_z = 0$; 180° is when IMF $B_y = 0$ and IMF B_z is negative; and 270° is when IMF B_y is negative and IMF $B_z = 0$). As can be seen in the plots for the lobe data, typical θ_{IMF} probabilities peak almost equally at ~90° and 270° and have minimums at 0° and 180° with the difference between the maximum and minimum probabilities being less than a factor of 10. For the mantle plasma, depending on the (Y, Z) regions, θ_{IMF} peaks dominantly at either ~90° or ~270°. The least favorable IMF conditions for the appearance of the mantle plasma are when $|\text{IMF } B_z| >> |\text{IMF } B_y|$. But the probability quickly becomes higher when $|\text{IMF } B_y|$ becomes $\geq |\text{IMF } B_z|$ with a factor of almost 100 between the maximum and minimum probabilities. As is discussed in section 5, that the mantle plasma is less likely to be seen by ARTEMIS in the low-latitude magnetotail when the IMF is dominantly northward or southward is due to that both the cusp and magnetopause sources for mantle plasma are at high latitudes. However, the probabilities do not appear to be clearly different between the *N* and *S* IMF as concluded in the Hardy et al. study. One possible reason could be that their data for *S* IMF period corresponded to larger IMF B_y. There are more measurements in this study than in the Hardy et al. study, thus likely providing more reliable statistical results.

3.2. The Cross-Tail Profiles of the Mantle Plasma and Field Parameters

Pilipp and Morfill [1978] theoretically predicted the spatial distributions of the mantle plasma as a function of the cross-tail and downtail distances resulting from the parallel and perpendicular transport of particles coming from either the cusp or the magnetopause source. Compared with hotter particles from the sources, colder particles move tailward with smaller parallel speed and are thus able to drift more deeply into the magnetosphere. The model predicted quite different cross-tail profiles corresponding to the two sources. With the magnetopause source, density, temperature, and bulk velocity are the highest at the magnetopause and decrease with increasing cross-tail distance away from the magnetopause. On the other hand, the density with the cusp source is significantly lower than that from the magnetopause source and the density

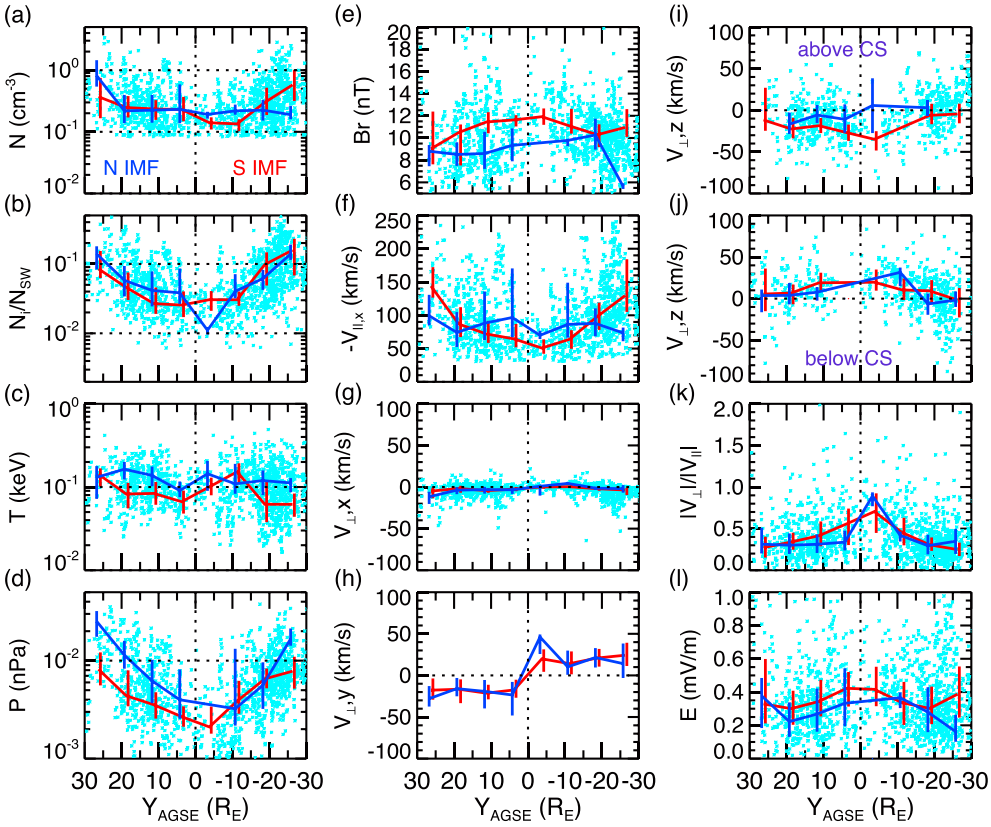

Figure 5. (a) Density, (b) density normalized to the solar wind density, (c) temperature, (d) plasma pressure, (e) magnetic field radial component strength, (f) $V_{||}$ in the $-X$ direction, (g) $V_{\perp,x}$, (h) $V_{\perp,y}$, (i) $V_{\perp,z}$ above the current sheet, (j) $V_{\perp,z}$ below the current sheet, (k) the $|V_\perp|$ to $|V_{||}|$ ratio, and (l) the convection electric field. The light blue dots are the mantle plasma data points for all IMF conditions (only every other 10 points are plotted for clarity). The red (blue) curves indicate the medians for *S* IMF (*N* IMF), and the vertical lines indicate the 25% and 75% quartiles.

peak at large downtail distance is displaced from the magnetopause. These predicted cross-tail profiles have not been appropriately evaluated. In this section we examined how the plasma and field parameters observed by ARTEMIS vary across the magnetotail.

Figure 5 shows the cross-tail distributions of the plasma moments and magnetic and electric fields for all the mantle plasma data (the blue dots, including data points from both above and below the current sheet), as well as the medians and quartiles of data corresponding to either *N* or *S* IMF conditions. Under *S* IMF, the normalized density, plasma pressure, and $V_{||}$ decrease with decreasing $|Y|$ by a factor of ~5 (for density) and ~3 (for pressure and $V_{||}$) from the flanks to midnight while the temperature has no clear *Y* dependence. The magnetic field in the mantles is mainly directed along the *X* direction, and the magnetic field strength is slightly larger near midnight than near flanks, opposite to the profile of plasma pressure. $V_\perp$ is mainly directed in the *Y* and *Z* directions. $V_{\perp,y}$ in the premidnight (postmidnight) sector is negative (positive), while $V_{\perp,z}$ in the region above (below) the current sheet is negative (positive). The $V_\perp$ speed is smaller than the $V_{||}$ speed, and the $|V_\perp|$ to $|V_{||}|$ speed ratio increases with decreasing $|Y|$ mainly due to the decrease of $|V_{||}|$. Since $V_\perp$ magnitudes do not change substantially with *Y*, the convection electric field ($E = |V_\perp \times B|$) becomes larger at smaller $|Y|$. The above profiles indicate that as the mantle plasma flows tailward along the field lines, it also drifts toward midnight and toward the current sheet with its density decreasing as it drifts deeper into the magnetotail.

The cross-tail profiles for some parameters are found to be substantially different between the *N* and *S* IMF conditions. Compared with those under *S* IMF, density under *N* IMF is similar while temperature and pressure are higher. In response to the higher pressure, magnetic field strength becomes smaller. The $V_{||}$ profile becomes flatter with the speed near midnight (the flanks) becoming larger (lower). The $V_{\perp,z}$ speed drops while the $V_{\perp,y}$ speed has little change. The lower magnetic field strength and $V_\perp$ speed indicate smaller convection *E* during *N* IMF.

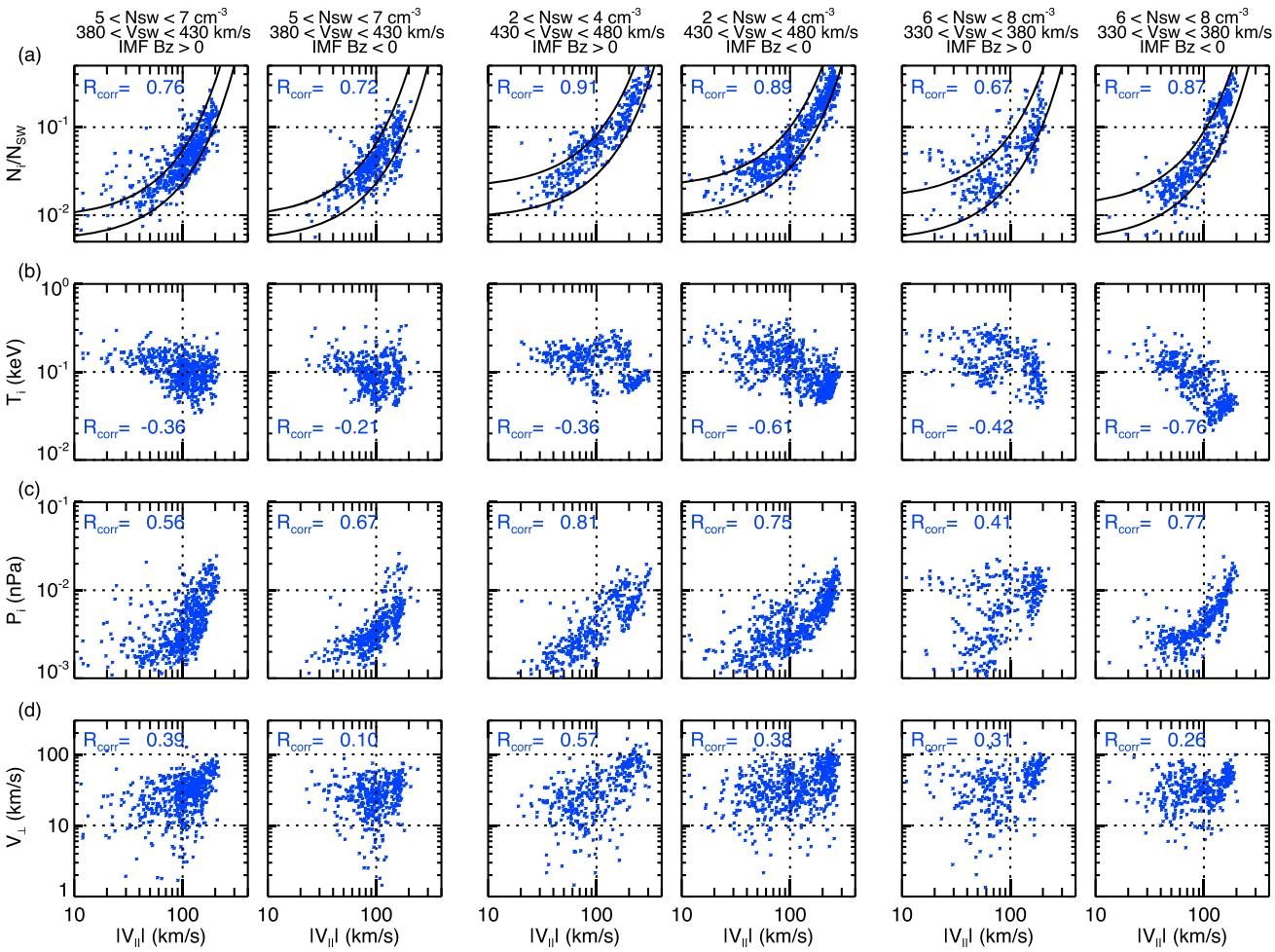

Figure 6. (a) Density normalized to the solar wind density, (b) temperature, (c) plasma pressure, and (d) $|V_{\perp}|$ as a function of $|V_{||}|$ for all mantle data under different ranges of solar wind density (N_{sw}) and solar wind speed (V_{sw}) for IMF $B_z > 0$ and IMF $B_z < 0$ as indicated on the top of each column. R_{corr} is the linear correlation coefficient. The two black lines in each N/N_{sw} versus $|V_{||}|$ plot shown in Figure 6a indicate the lower and upper limits of the mantle density as described in the text.

The *Y* profiles of density and velocity are more consistent with the *Pilipp and Morfill* [1978] profiles for the magnetopause source than for the cusp source, suggesting that the observed mantle plasma mainly comes from the magnetopause source extending continuously down the magnetotail. These profiles are also qualitatively consistent with the MHD predictions presented in section 4. However, there is inconsistency between the observed temperature profiles and those predicted by the Pilipp and Morfill and MHD models, which we will discuss in section 5.2.

3.3. Correlations of the Mantle Plasma Parameters With $V_{||}$

The 1-D MHD simulation [*Siscoe and Sanchez*, 1987; *Siscoe et al*., 1994] predicted that as the density and tailward speed of the mantle plasma change with changing upstream solar wind speeds, the mantle density and the $V_{||}$ speed remain strongly and monotonically correlated. The strong density-$V_{||}$ correlation has been observed in both the near-Earth [*Taguchi et al*., 2001] and distant tail [*Siscoe et al*., 1994; *Maezawa and Hori*, 1998]. Here we evaluated this correlation with ARTEMIS statistical results and also examined how the $V_{||}$ speed is correlated with other plasma parameters.

Figure 6 shows the variations of normalized density, temperature, plasma pressure, and $|V_{\perp}|$ with $|V_{||}|$ under different ranges of solar wind density and speed for the *N* and *S* IMF conditions. Both density and pressure are highly correlated with $|V_{||}|$ with higher positive correlations with density. The correlation with density is consistent with the 1-D MHD prediction above. It can be seen in Figure 6a that the majority of the data points

falls between a lower and an upper limit lines indicated by the black lines. The logarithm of the density limit is thus a linear function of the $V_{||}$ speed ($\log_{10}(N) = \log_{10}(N_0) + C \cdot |V_{||}|$, where N_0 is the density limit). The constants N_0 and C are different for the two limits, and their values also change with the solar wind density, speed, and IMF B_z. Thus, we use this density-$V_{||}$ correlation in section 4 to identify the mantle plasma in the global MHD simulations. Temperature, on the other hand, is anticorrelated with $|V_{||}|$. $|V_{\perp}|$ is, in general, larger when $|V_{||}|$ is larger, but the correlations are weaker than those seen in density and pressure. These correlations do not vary clearly with the IMF B_z direction. In section 4, we further compare these observed correlations with those predicted by a global MHD.

4. Global MHD Simulations

The past modeling and simulation works mentioned in section 1, despite using simplified assumptions or simulation conditions, have provided us some basic understanding of the formation of the mantle plasma. In this section we examine the predictions from more realistic simulations with the BATS-R-US global MHD model and investigate factors that affect the spatial distributions of the mantle plasma, particularly their dependencies on IMF B_y and B_z conditions.

4.1. Simulation Setups

BATS-R-US is a global model that employs ideal single-fluid MHD equations to describe the solar wind-magnetosphere-ionosphere interaction [*Powell et al*., 1999; *Tóth et al*., 2012]. The BATS-R-US results presented here are obtained from the simulations conducted at the Community Coordinated Modeling Center (CCMC) at NASA Goddard Space Fight Center. We investigate five simulation runs (see the Acknowledgment) with different IMF clock angles ($\theta_{IMF} = 0°$, 45°, 90°, 135°, and 180°). Each simulation was run under steady upstream solar wind and IMF conditions: IMF = 7.15 nT, $V_{SW} = V_{SW,\,x} = -560$ km/s, $N_{SW} = 3.3\ \mathrm{cm}^{-3}$, and $T_{SW} = 116{,}040$ K with 0° dipole tilt angle. The MHD equations are solved on a three-dimensional block adaptive Cartesian grid. The simulation domain is $32 > X > -224\ R_E$ and $128 > Y\,(Z) > -128\ R_E$. Grid cell sizes are $0.25 \times 0.25 \times 0.25\ R_E^3$ in the region of $|X|$, $|Y|$, and $|Z| < 8\ R_E$ and $0.5 \times 0.5 \times 0.5\ R_E^3$ in the remainder of the simulation domain. The near-Earth inner boundary of the code at 3 R_E from the Earth is handled by incorporating a coupled model for the ionospheric electric field [*Ridley et al*., 2004]. Field-aligned currents are calculated and mapped along dipole field lines to the ionosphere where they are used as the source term for the height-integrated potential equation. The calculated potential is then mapped back out to the inner boundary where it is used to determine boundary conditions for the velocity and electric field. The ionosphere comprises a two-dimensional layer with prescribed finite Pedersen and Hall conductances [*Gombosi et al*., 2000]. In these simulations, uniform Hall and Pedersen conductances of 5 mhos were specified. Ionospheric outflow can be included in the BATS-R-US simulations, but we specified no ionospheric outflow in our simulation. Note that the simulations have an inner plasma boundary condition with density ~30 cm^{-3} and temperature ~2 eV being specified everywhere at the boundary. This plasma can diffuse into the inner magnetosphere even if the radial velocity at the inner boundary is set to zero, but it is not expected to contribute to the mantle plasma in the magnetotail presented in this study.

4.2. Simulation Results

Figure 7a shows the *Y-Z* profiles of the simulated perpendicular current density ($|J_{\perp}|$) at $X = -60\ R_E$ for the five clock angles. The current is large along the magnetopause and in the current sheet. Outside the magnetopause, the magnetosheath plasma flows tailward in the perpendicular direction. Using these characteristics, we selected the lobe region as having $V_{\perp,\,x} \geq -100$ km/s and $|J_{\perp}| \leq 7\ 10^{-5}\ \mu\mathrm{A/m}^2$. The density as a function of $V_{||}$ for plasma in the lobe region is shown in Figure 7c. It can be seen that there are two types of plasma: one has density highly and positively correlated with $V_{||}$, which we defined it as the mantle plasma, and the other does not, which we referred it to as the lobe plasma. When $\theta_{IMF} = 0$, no plasma that satisfies our mantle definition can be identified. The positive density-$V_{||}$ correlation for the mantle plasma has been demonstrated in the past MHD simulations [e.g., *Siscoe and Sanchez*, 1987; *Siscoe et al*., 1994]. It can be seen in Figure 7c, like the ARTEMIS densities shown in Figure 6a, that the simulated densities also fall between a lower and an upper limit lines indicated by the black dotted lines with logarithm of the density limit being a linear function of $|V_{||}|$ (the constants N_0 and C are different for the two limits and their values also change with X and θ_{IMF}). By finding the two limit lines, together with the requirement of tailward flow along

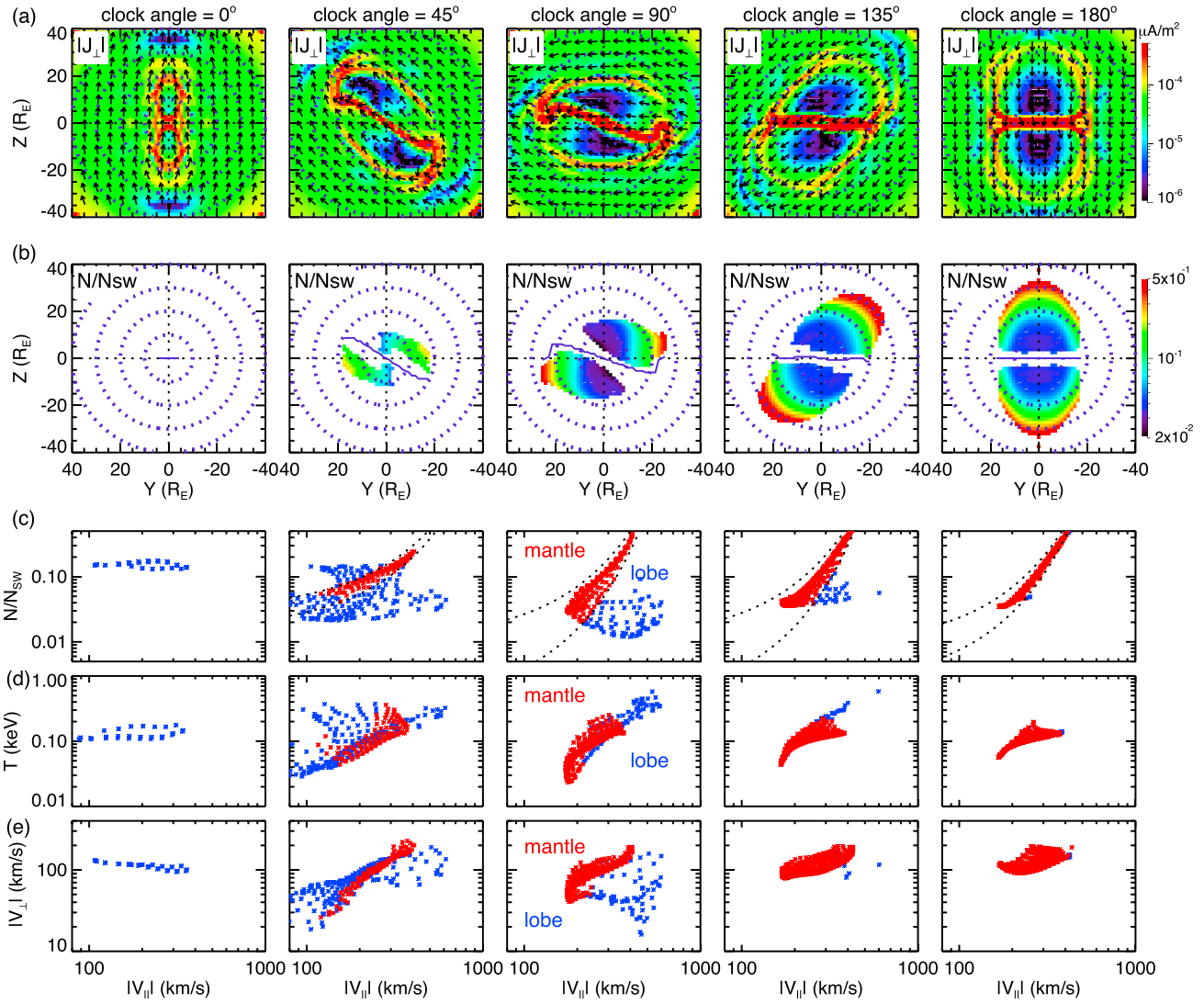

Figure 7. The *Y-Z* distributions of (a) $|J_\perp|$ and (b) mantle density normalized to the solar wind density at $X = -60\ R_E$ under five different clock angles indicated on the top of each column. The black arrows in Figure 7a are the magnetic field vectors in the *Y-Z* plane. The purple solid curves in Figure 7b indicate the center of the current sheet. (c) The normalized density, (d) temperature, and (e) $|V_\perp|$ as a function of $|V_{||}|$ for plasma in the lobe region. The red (blue) dots indicate the mantle (lobe) plasma. The two black dotted lines in each N/N_{sw} versus $|V_{||}|$ plot (except for the clock angle = 0) indicate the lower and upper limits of the mantle density that are described in the text.

the magnetic field, allows us to separate the mantle plasma from the lobe plasma. Figure 7d shows that the mantle temperature is also positively correlated with $V_{||}$, which is not seen in the observations shown in Figure 6b. On the other hand, the $V_\perp$-$V_{||}$ correlations are qualitatively consistent with the observed correlations shown in Figure 6d. The correlations with $V_{||}$ are stronger for density and temperature but weaker for $V_\perp$ during *S* IMF than *N* IMF.

The spatial distributions of the normalized mantle plasma density are shown in Figure 7b. The distributions in the region above or below the current sheet have clear dawn-dusk asymmetries when there is an IMF B_y component. The mantle density is the highest just inside the magnetopause at a location where the magnetopause current density is the weakest. The location is presumably the site where magnetosheath plasma gets access to the magnetosphere through the open field lines. The density and temperature of the mantle plasma have their maximum values just inside the entry sites, and these values are almost the same as those of the magnetosheath plasma just outside the site. Thus, the locations of the maximum mantle density can be regarded as the magnetopause source locations for the mantle plasma. When |IMF B_y|

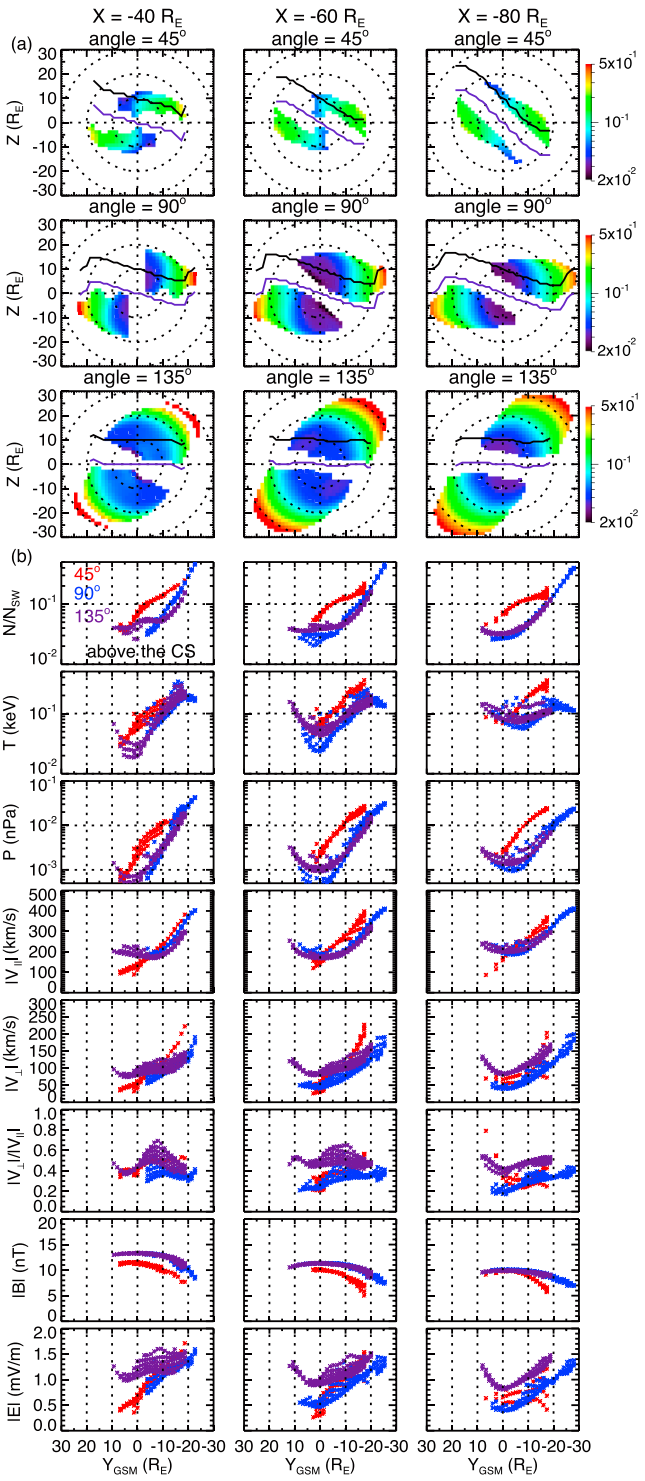

Figure 8. (a) The *Y-Z* distributions of mantle density normalized to the solar wind density at $X = -40$ (left column), -60 (middle column), and -80 R_E (right column) under three different clock angles. The solid purple curves indicate the center of the current sheet, and the solid black curves mark 10 R_E above the solid purple curves. (b) Plasma and field parameters associated with the mantle plasma above the current sheet within the region between the solid purple and black curves shown in Figure 8a for $\theta_{IMF} = 45°$ (the red dots), 90° (the blue dots), and 135° (the purple dots).

becomes $\geq |$IMF $B_z|$, the source locations clearly move to lower latitudes and to the opposite sides of the magnetosphere above and below the current sheet. This dawn-dusk asymmetry associated with the IMF B_y is explained in *Cowley* [1981]. The source latitudes, under the same IMF B_y, are lower during *N* IMF than *S* IMF. The dawn-dusk asymmetry is a result of nonzero IMF B_y, consistent with the IMF dependencies of the observed dawn-dusk asymmetries in the occurrence rates shown in Figure 3.

As indicated by the current density shown in Figure 7a, the cross section of the magnetopause is no longer a cylinder shape at this tail distance. It elongates to an elliptical shape with its long axis being roughly parallel to the IMF B_{yz} direction. The current sheet also tilts with respect to the long axis (the dipole title angle is set to 0). These magnetopause and current sheet reconfigurations change the relative distances between the source locations and the current sheet, thus affecting the mantle distributions near the current sheet. This is further discussed in section 5.1.

Figure 8a shows the *Y-Z* distributions of the normalized mantle density at different downtail distances for $\theta_{IMF} = 45°$, 90°, and 135°. To show how the plasma and field parameters associated with the mantle plasma in the vicinity of the current sheet vary across the tail, we plot in Figure 8b the *Y* profiles of these parameters within the region of 10 R_E above the current sheet (the region sandwiched by the solid purple and black curves, with 10 R_E being chosen to be consistent with the *Z* range covered by ARTEMIS as shown in Figure 2). Compared with *S* IMF, during *N* IMF the long axis of the elliptical magnetopause becoming parallel to the IMF B_{yz} direction occurs at larger downtail distances.

Across the tail above the current sheet, the mantle plasma density, temperature, and pressure decrease with decreasing $|Y|$ while the magnetic

field strength increases to maintain constant total pressure (plasma pressure + magnetic pressure). Both the $V_\perp$ and $V_{||}$ speeds weaken quickly toward smaller $|Y|$, while the ratios of these two speeds vary only slightly. The convection electric field ($E = |V_\perp \times B|$) becomes weaker at smaller $|Y|$. Generally, these Y profiles tend to become flatter with increasing downtail distances. These Y variations are qualitatively consistent with the ARTEMIS profiles shown in Figure 5 in density, pressure, magnetic field strength, and $V_{||}$, but not in temperature, $V_\perp$, and E.

In the MHD results, the mantle plasma moments and fields near the current sheet are substantially different between N and S IMF, with density, temperature, and pressure being higher while magnetic field and electric field strengths being lower during N IMF. Both the $V_{||}$ and $V_\perp$ speeds become larger near the flanks but smaller at midnight during N IMF. Similar IMF B_z dependencies are seen in the observed profiles for temperature, pressure, magnetic field, and electric field strengths shown in Figure 5. However, the ARTEMIS profiles show no substantial density changes with the IMF B_z direction, which appears to be qualitatively different from the MHD results.

Note that the inconsistencies in the above model-observation comparisons may simply be due to that the MHD profiles are from steady mantle distributions resulting from the steady solar wind and IMF conditions specified while the statistical ARTEMIS results include data from the mantle plasma evolving under a variety of time-varying solar wind and IMF conditions. As indicated by the MHD results, the mantle plasma and fields vary significantly with the IMF B_z and downtail distances. To examine this factor, we have also sorted the mantle density using 10 h averaged IMF B_z, which should better represent the effect under a long-period of steady IMF than does using 4 h averaged IMF B_z shown in Figure 5. We found that density near midnight is higher when the 10 h averaged IMF is northward, more consistent with the MHD results shown in Figure 8. Thus, in a future study, statistical analysis of the results from a MHD simulation over a considerately longer period with realistic solar wind and IMF variations should provide more appropriate comparisons with the ARTEMIS results.

5. Discussion

5.1. Effect of IMF B_y and IMF B_z on the Mantle Distributions

The appearance and density of the mantle plasma just outside the current sheet indicate the strength of the particle supply into the plasma sheet, which is determined by the factors of the locations and strengths of the sources, the distance from the sources to the current sheet, and the parallel and perpendicular velocities. *Hardy et al*. [1976], without considering the changes in the source strengths and locations, speculated that the observed dawn-dusk asymmetric mantle appearance corresponding to the IMF B_y direction at lunar distances is a result of a dawn-dusk asymmetry in the perpendicular speed. Higher perpendicular speed on the side where the magnetic field has a component parallel to the IMF would allow the mantle plasma to reach closer to the current sheet on that side. However, as indicated by the MHD results shown in Figures 7 and 8, both the strength of the magnetopause source and its location relative to the current sheet vary significantly in the magnetotail with IMF B_y and B_z as a result of changes in the magnetopause cross-section shape and tilt of the current sheet.

When there is IMF B_y, the magnetopause becomes elliptical and the current sheet tilts [*Sibeck and Lin*, 2014; *Wang et al*., 2014]. The elliptical magnetopause elongates along the direction of IMF, as a result of the anisotropic pressure of draped magnetosheath magnetic field lines [*Michel and Dessler*, 1970] and the inclusion of a reconnection-generated standing slow mode wave fan bounded by a rotational discontinuity [e.g., *Siscoe and Sanchez*, 1987]. Dawn-dusk asymmetric penetration of IMF into the lobes above and below the current sheet causes the current sheet to tilt away from the long axis of the elliptical magnetopause. Details of the magnetopause shapes and the current sheet tilting for the BATS-R-US simulations similar to those presented in section 4 are discussed in *Sibeck and Lin* [2014]. Their results also show that the elongation and current sheet tilting at lunar distances are more significant when the IMF magnitude is larger and that it takes 10–20 min for the cross-section configuration to adjust in response to an IMF direction change.

As shown in Figure 7, the magnetopause source locations are closer to the long elliptical axis than to the short axis. Under the same IMF B_y, the alignment of the long axis with the IMF direction moves the magnetopause source locations to smaller $|Z|$ and $|Y|$ during N IMF than S IMF. For example, the source location at $X = -60\ R_E$

is located at $|Z|$ ~0 (20) R_E and $|Y|$ ~17 (22) R_E for $\theta_{IMF} = 45°$ (135°). The current sheet tilts farther away from the long axis during *S* IMF than *N* IMF. As a result, the source becomes closer to the current sheet and midnight during *N* IMF than *S* IMF. The ratios of the perpendicular to parallel speed do not change significantly with the IMF B_z direction. Thus, despite the source strength being higher during *S* IMF than *N* IMF (N/N_{sw} ~0.2 for *N* IMF and ~0.5 for *S* IMF, as seen in Figure 7), the shorter distance from the source to the current sheet results in higher mantle density near the current sheet under *N* IMF in these simulations. How these factors and their combined effects vary with IMF B_y and B_z under different solar wind densities and speeds and IMF magnitudes should be further investigated in the future.

5.2. Mixture of the Mantle Plasma With Plasma From the Plasma Sheet or PSBL

A significant difference between the above observation and simulation results is seen in temperature in both its cross-tail profiles and its correlations with density and $V_{||}$. The reason is that it is not unusual for the ARTEMIS probes, being at low latitudes in the vicinity of the current sheet, to observe cold mantle plasma coexisting with hotter plasma of the plasma sheet energy or/and with the hotter plasma from the plasma sheet boundary layer (PSBL). Thus, when computing the plasma moments from this particle distribution of mixed populations, the temperature is higher than that of the mantle population alone. The mixture of the mantle plasma with the plasma sheet or PSBL plasma, which has been observed in the near-Earth tail [*Akinrimisi et al*., 1990] and distant tail [*Maezawa and Hori*, 1998], strongly indicates that the mantle is a supplier of plasma to the plasma sheet.

Figure 9a shows an example of such mixture as ARTEMIS-B moved from the magnetosheath to the mantle (it crossed the magnetopause at ~1700 UT). In the mantle from 1700 to 1718 UT, density, $V_{||}$, and temperature all decreased together, which is consistent with the model prediction. After 1718 UT, density and $V_{||}$ continued to decrease while temperature started to increase due to an increase in the particle fluxes above 1 keV as can be seen in the energy spectrum of omnidirectional particle energy fluxes. (Note that the energy of the peak of omnidirectional energy fluxes becomes higher than the thermal energy due to the shift of the phase space density with bulk velocity. For example, in the sheath, the thermal energy is ~0.1 keV, but the strong bulk velocity of ~300 km/s shifts the peak of omnidirectional flux to ~1 keV.) The 2-D gyroaveraged phase space density (PSD) distributions on the $V_{||}$-$V_{\perp}$ plane at four different selected times (16:46 UT for the magnetosheath, 17:06 and 17:18 UT for the mantle, and 17:44 UT for mixture of mantle and hot plasma) are shown in Figure 9b. The peak of PSD in all plots is shifted toward $-V_{||}$, indicating the tail flowing sheath or mantle plasma (the peak of the sheath PSD is also shifted toward $-V_{\perp}$). The shift can be more clearly seen in the 1-D PSD distributions cut at $V_{\perp} = 0$ as a function of $V_{||}$ shown in Figure 9c. Comparing the PSD at 17:44 UT with those at 17:06 and 17:18 UT, there are significantly more particles at higher energies (a proton with velocity of 300 (600) km/s corresponds to 0.468 (1.875) keV), especially in the perpendicular direction. The increase in the number of higher-energy particles can be more clearly seen in the normalized and shifted 1-D PSD distributions (normalized to its peak value and with its peak shifted to $V_{||} = 0$) as shown in Figure 9d.

Figures 9e to 9h show an example of mixture of the mantle plasma with the PSBL plasma observed by ARTEMIS-B as it moved from the mantle to the plasma sheet. The earthward flowing PSBL population can be seen in the PSD plots of 16:05 and 16:08 UT coexisting with the tailward flowing mantle population. In the 16:05 UT plot, part of the PSBL population that is mirrored back from the Earth and flowing tailward can also be seen at $V_{||} \sim -900$ km/s. These PSBL signatures are consistent with the simulated PSD distributions of the particles under Speiser motion in the current sheet [*Ashour-Abdalla et al*., 1996]. Thus, the mixture with PSBL also suggests that the mantle plasma has entered the closed field line region. The mixture with the PSBL plasma results in higher temperature but reduced tailward $V_{||}$ speed, since the main PSBL population moves along the field lines in the direction opposite to that of the mantle plasma.

5.3. Flow Fluctuation and Diffusive Transport

The perpendicular flows shown in Figure 5 bring the mantle plasma toward midnight and the current sheet, but $V_{\perp, z}$ can become very small during *N* IMF. Figure 10 shows an example of the flows, magnetic field strength, and density associated with the mantle plasma during a prolonged *N* IMF period. As shown in Figures 10a to 10c, during this period the solar wind density, slow wind speed (not shown, ~400 km/s), and IMF are relatively steady and geomagnetic activity is very low. Figure 10d shows that $V_{||}$ varies from 50 to 150 km/s while $V_{\perp}$ is less than 50 km/s. However, Figure 10e shows that *V* fluctuates significantly with a

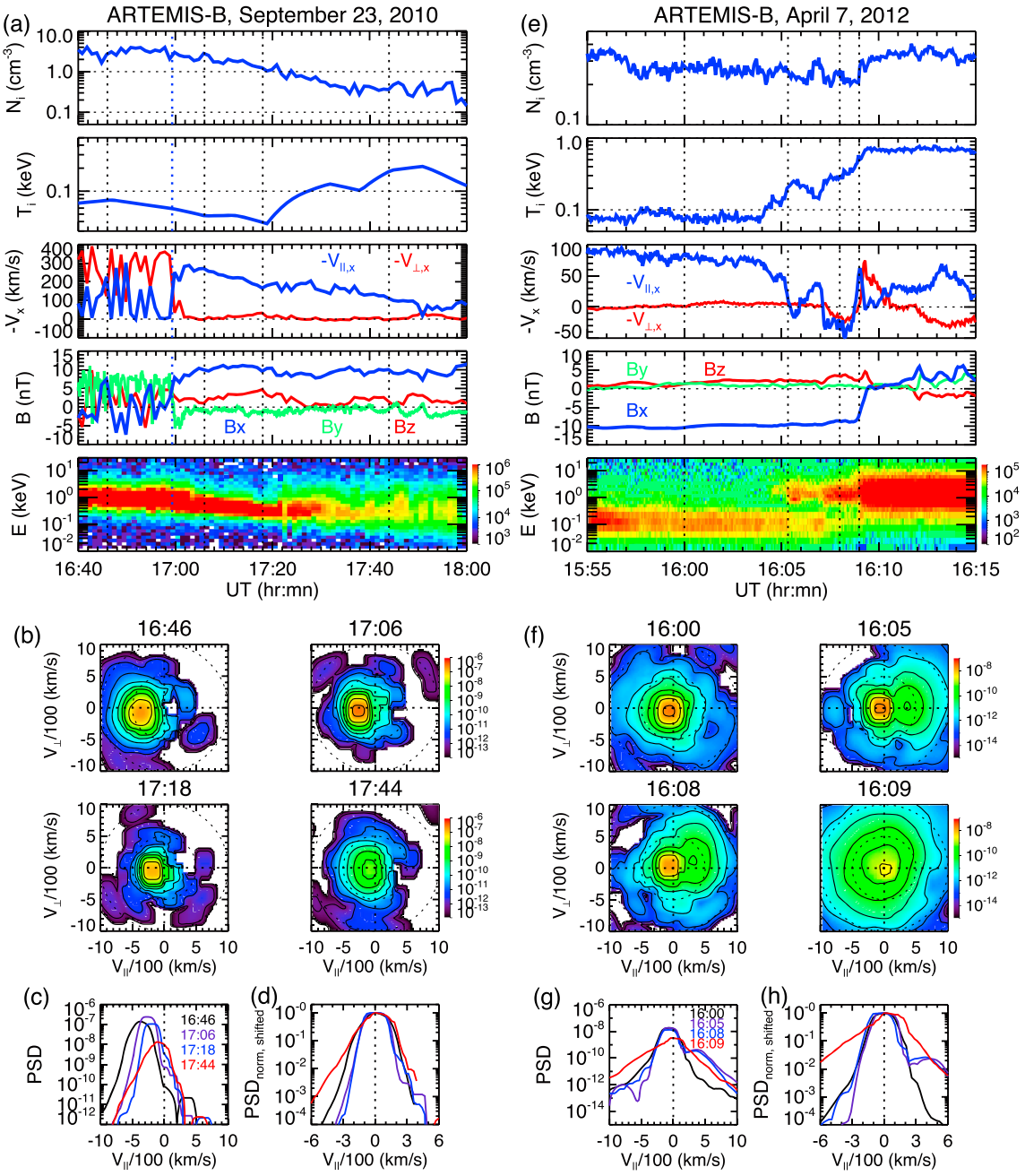

Figure 9. (a) Density, temperature, bulk velocities, magnetic fields, and energy fluxes (eV/(s sr cm^2 eV)) observed by ARTEMIS-B on 23 September 2010. (b) Gyroaveraged phase space density (s^3/km^3/cm^3) in the $V_{||}$-$V_{\perp}$ plane for four different times indicated on the top of each plot. (c) One-dimensional cut of the 2-D plots shown in Figure 9b at $V_{\perp}=0$. (d) The phase space density profiles shown in Figure 9c normalized to their peaks and with the peaks shifted to $V_{||}=0$. (e–h) The ARTEMIS-B observations on 7 April 2012.

timescale of approximately a few to 10 min in its magnitude and direction with the fluctuation magnitude much larger than its 20 min averages. The fluctuation/average ratios shown in Figure 10f are significantly larger in $V_{\perp}$ than in other parameters. The small fluctuations in $|B|$ indicate that the $V_{\perp}$ fluctuations are due to the fluctuations in convection electric field.

The perpendicular flow fluctuations have been observed by Cluster in the near-Earth lobes [*Förster et al.*, 2007], in the ionosphere by radars [*Bristow*, 2008], and in the plasma sheet by various satellites [e.g., *Angelopoulos et al.*, 1993; *Borovsky et al.*, 1997; *Wang et al.*, 2010; *Stepanova et al.*, 2011]. When there is a

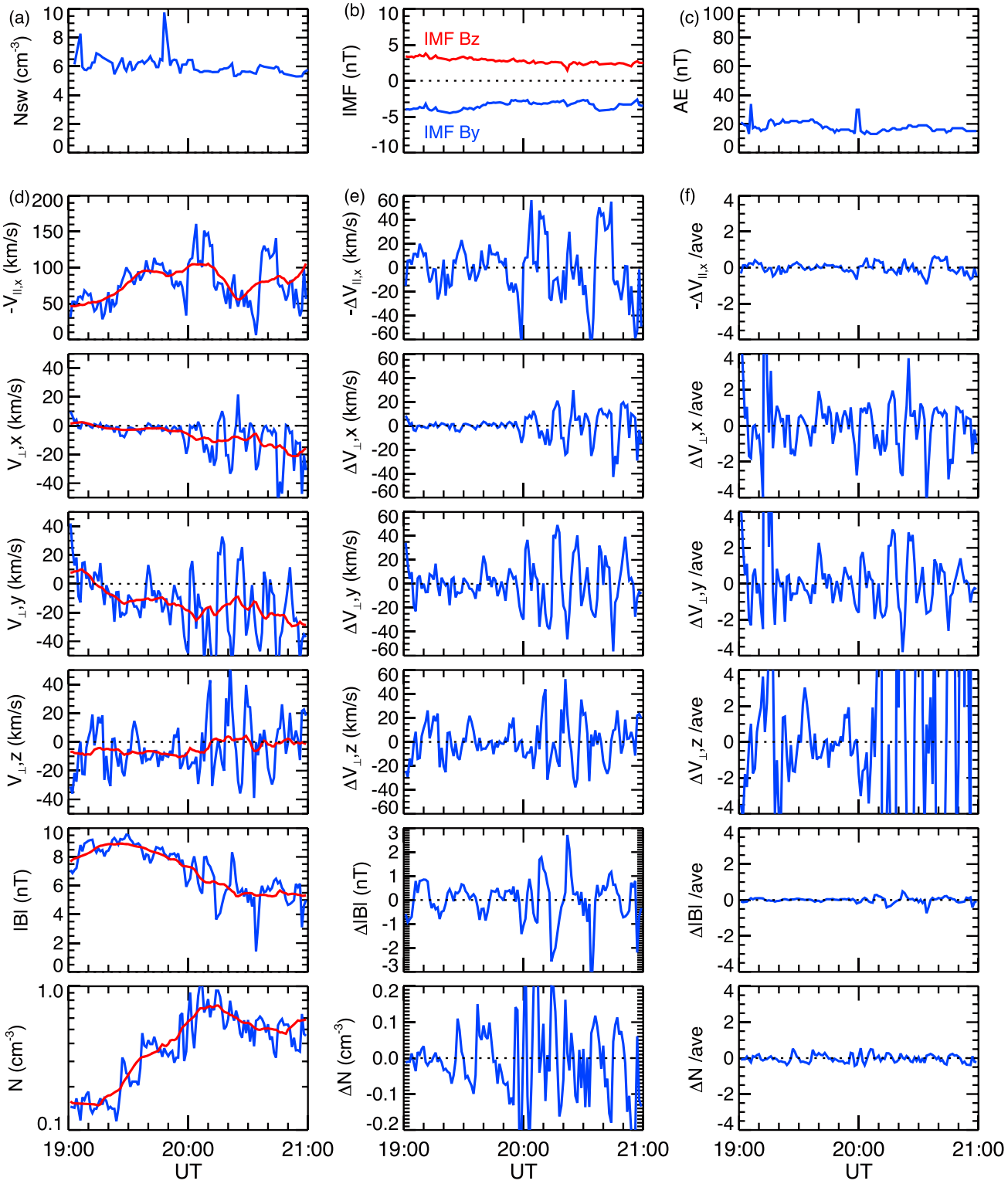

Figure 10. (a) The solar wind density, (b) IMF B_y and B_z (including 22 min delay from the bow shock nose to the probe location), and (c) *AE* from 19 to 21 UT on 19 November 2010. (d) The bulk velocities, magnetic field strength, and density observed by ARTEMIS-B (the blue curves) and their 20 min running averages (the red curves). (e) The differences from the averages. (f) The ratios of the differences to the averages.

spatial gradient of plasma density, flow fluctuations can result in diffusive transport [e.g., *Angelopoulos et al*., 1994; *Borovsky et al*., 1997; *Antonova*, 2005]. *Wang et al*. [2010] showed that diffusive transport in the plasma sheet can move cold particles across the tail when average drift flow becomes small during *N* IMF to account for the observed formation of cold and dense plasma sheet. Therefore, as shown in Figure 10, despite the average $V_{\perp,\,z}$ remaining nearly zero during the period, it is very likely that the strong fluctuations can still continue to diffuse mantle plasma toward the current sheet.

6. Summary

To understand the plasma supply from the mantle into the plasma sheet in the magnetotail, we statistically investigated the characteristics and cross-tail distributions of the plasma and field parameters associated with the low-latitude mantle plasma and their dependencies on the IMF direction observed by ARTEMIS between $-40 > X > -80\ R_E$. We also investigated the factors controlling the mantle distributions predicted by BATS-R-US global MHD simulations.

The observations show that the mantle plasma flows tailward along magnetic field lines with substantial $V_{||}$ speed from ~50 to 200 km/s and at the same time drifts toward midnight and toward the current sheet with drift speed less than ~50% of the parallel speed. Its density is about an order of magnitude lower than in the magnetosheath but is similar to that in the plasma sheet. The density is highly and positively correlated with the $V_{||}$ speed. The temperature is similar to that in the magnetosheath but is lower than in the plasma sheet. The observations show clear dawn-dusk asymmetries in the mantle appearance, with higher occurrence rates in the postmidnight (premidnight) sector above the current sheet when IMF B_y is positive (negative). Opposite dawn-dusk asymmetries are seen below the current sheet. The occurrence rates, density, and $V_{||}$ all decrease with decreasing $|Y|$. This observed density cross-tail profile is qualitatively consistent with the cross-tail density profiles resulting from the magnetopause source predicted by *Pilipp and Morfill* [1978] and with those from the BATS-R-US simulations, indicating that the magnetosheath plasma entering through the tail magnetopause along the open field line is an important source for the mantle plasma and the source likely exists continuously down the tail.

It is not unusual for the ARTEMIS probes in the vicinity of the current sheet to observe the mantle plasma mixed with higher-energy particles from the plasma sheet or the PSBL, indicating that the mantle plasma likely has entered a region of newly closed field lines. Future studies of these mixtures observed by ARTEMIS should provide more understanding of the plasma entry from the mantles to the plasma sheet. The drift toward the current sheet becomes quite small during *N* IMF. However, the drift can be highly fluctuating with fluctuation speed significantly larger than the averaged drift speed. This may lead to diffusive transport that brings the mantle plasma into the current sheet.

The BATS-R-US MHD results indicate that as IMF B_y becomes dominant, the mantle source locations move to lower latitudes and become dawn-dusk asymmetric, leading to the dawn-dusk asymmetry of the mantle appearance. The tail cross-section configuration in the magnetotail is distorted. The magnetopause shape becomes elliptical with its long axis roughly along the IMF B_{yz} direction and the current sheet becomes tilted from the long axis, thus altering the distance from the magnetopause source to the current sheet. The source strength is stronger, but its distance to the current becomes larger during *S* IMF than *N* IMF, leading to smaller mantle density near the current sheet.

Acknowledgments

The work by C.-P. Wang and L.R. Lyons has been supported by NASA grant NNX11AJ12G and NSF grant ATM-1003595. We acknowledge NASA contract NAS5-02099 for ARTEMIS and C.W. Carlson and J.P. McFadden for the use of ESA data, D. Larson and R.P. Lin for use of the SST data, and K.H. Glassmeier, U. Auster, and W. Baumjohann for the use of FGM data provided under DLR contract 50 OC 0302. The ARTEMIS data are available online (http://artemis.ssl.berkeley.edu/) for free. Simulation results have been provided by the Community Coordinated Modeling Center (CCMC) free of charge at Goddard Space Flight Center through their public Runs on Request system (http://ccmc.gsfc.nasa.gov). In particular, we have studied the runs "Claire_Kuang_071X11_X." The BATS-R-US model was developed by the CSEM group at the University of Michigan. We thank T. Gombosi at the University of Michigan for helpful discussion of the simulation results. We thank A. Poppe at the University of California at Berkeley for discussion of lunar pickup ions. We thank J.H. King, N. Papatashvilli at AdnetSystems, NASA GSFC, and CDAWeb for providing the OMNI data. We thank the support of ISSI International Teams Program: Plasma Entry and Transport in the Plasma Sheet.

Michael Liemohn thanks Elizaveta Antonova and another reviewer for their assistance in evaluating the paper.

References

Akinrimisi, J., S. Orsini, M. Candidi, and H. Balsiger (1990), Ion dynamics in the plasma mantle, *Ann. Geophys.*, *8*, 739–754.

André, M., and C. M. Cully (2012), Low-energy ions: A previously hidden solar system particle population, *Geophys. Res. Lett.*, *39*, L03101, doi:10.1029/2011GL050242.

Angelopoulos, V., et al. (1993), Characteristics of ion flow in the quiet state of the inner plasma sheet, *Geophys. Res. Lett.*, *20*, 1711–1714, doi:10.1029/93GL00847.

Angelopoulos, V., T. Mukai, and S. Kokubun (1994), Evidence for intermittency in Earth's plasma sheet and implications for self-organized criticality, *Phys. Plasmas*, *6*, 4161, doi:10.1063/1.873681.

Antonova, E. E. (2005), The structure of the magnetospheric boundary layers and the magnetospheric turbulence, *Planet. Space Sci.*, *53*, 161–168, doi:10.1016/j.pss.2004.09.041.

Ashour-Abdalla, M., L. A. Frank, W. R. Paterson, V. Peroomian, and L. M. Zelenyi (1996), Proton velocity distributions in the magnetotail: Theory and observations, *J. Geophys. Res.*, *101*, 2587–2598, doi:10.1029/95JA02539.

Auster, H. U., et al. (2008), The THEMIS fluxgate magnetometer, *Space Sci. Rev.*, *141*, 235–264, doi:10.1007/s11214-008-9365-9.

Borovsky, J., R. C. Elphic, H. O. Funsten, and M. F. Thomsen (1997), The Earth's plasma sheet as a laboratory for flow turbulence in high-β MHD, *J. Plasma Phys.*, *57*, 1–34, doi:10.1017/S0022377896005259.

Bristow, W. (2008), Statistics of velocity fluctuations observed by SuperDARN under steady interplanetary magnetic field conditions, *J. Geophys. Res.*, *113*, A11202, doi:10.1029/2008JA013203.

Candidi, M., S. Orsini, and V. Formisano (1982), The properties of ionospheric O^+ ions as observed in the magnetotail boundary layer and northern plasma lobe, *J. Geophys. Res.*, *87*, 9097–9106, doi:10.1029/JA087iA11p09097.

Cowley, S. W. H. (1981), Magnetospheric asymmetries associated with the y-component of the IMF, *Planet. Space Sci.*, *29*, 79–96.

Engebretson, M. J., et al. (2012), Cluster observations of band-limited Pc 1 waves associated with streaming H^+ and O^+ ions in the high-altitude plasma mantle, *J. Geophys. Res.*, *117*, A10219, doi:10.1029/2012JA017982.

Förster, M., G. Paschmann, S. E. Haaland, J. M. Quinn, R. B. Torbert, H. Vaith, and C. A. Kletzing (2007), High-latitude plasma convection from Cluster EDI: Variances and solar wind correlations, *Ann. Geophys.*, *25*, 1691–1707, doi:10.5194/angeo-25-1691-2007.

Gombosi, T. I., D. L. DeZeeuw, C. P. T. Groth, and K. G. Powell (2000), Magnetospheric configuration for Parker-spiral IMF conditions: Results of a 3D AMR MHD simulation, *Adv. Space Res.*, *26*, 139–149, doi:10.1016/S0273-1177(99)01040-6.

Gosling, J. T., D. N. Baker, S. J. Bame, E. W. Hones Jr., D. J. McComas, R. D. Zwickl, J. A. Slavin, E. J. Smith, and B. T. Tsurutani (1984), Plasma entry into the distant tail lobes: ISEE-3, *Geophys. Res. Lett.*, *11*, 1078–1081, doi:10.1029/GL011i010p01078.

Grzedzielski, S., and W. Macek (1988), An open magnetopause model of the Earth's distant tail based on ISEE 3 evidence, *J. Geophys. Res.*, *93*, 1795–1808, doi:10.1029/JA093iA03p01795.

Haerendel, G., and G. Paschmann (1975), Entry of solar wind plasma into the magnetosphere, in *Physics of the Hot Plasma in the Magnetosphere*, edited by B. Hultqvist and L. Stenflo, pp. 23–43, Plenum, New York.

Hardy, D. A., H. K. Hills, and J. W. Freeman (1975), A new plasma regime in the distant geomagnetic tail, *Geophysical Research Letters*, *2*, 169–172, doi:10.1029/GL002i005p00169.

Hardy, D. A., J. W. Freeman, and H. K. Hills (1976), Plasma observations in the magnetotail, in *Magnetospheric Particles and Fields*, vol. 89, edited by B. M. McCormac, pp. 89–98, D. Reidel, Hingham, Mass, and Dordrecht, Netherlands.

Hardy, D. A., H. K. Hills, and J. W. Freeman (1979), Occurrence of the lobe plasma at lunar distance, *J. Geophys. Res.*, *84*, 72–78, doi:10.1029/JA084iA01p00072.

Hones, E. W., Jr., J. R. Asbridge, S. J. Bame, M. D. Montgomery, S. Singer, and S.-I. Akasofu (1972), Measurements of magnetotail plasma flow made with Vela 4B, *J. Geophys. Res.*, *77*, 5503–5522, doi:10.1029/JA077i028p05503.

Iglewicz, B., and D. Hoaglin (1993), How to detect and handle outliers, in *The ASQC Basic References in Quality Control: Statistical Techniques*, vol. 16, edited by E. F. Mykytka, 87 pp., ASQC Quality Press, Milwaukee, Wis.

Maezawa, K., and T. Hori (1998), The distant magnetotail: Its structure, IMF dependence, and thermal properties, in *New Perspectives on the Earth's Magnetotail*, *Geophys. Monogr. Ser.*, vol. 105, edited by A. Nishida, D. N. Baker, and S. W. H. Cowley, pp. 1–20, AGU, Washington, D. C.

McFadden, J. P., C. W. Carlson, D. Larson, V. Angelopoulos, M. Ludlam, R. Abiad, B. Elliott, P. Turin, and M. Marckwordt (2008), The THEMIS ESA plasma instrument and in-flight calibration, *Space Sci. Rev.*, *141*, 277–302, doi:10.1007/s11214-008-9440-2.

Michel, F. C., and A. J. Dessler (1970), Diffusive entry of solar-flare particles into geomagnetic tail, *J. Geophys. Res.*, *75*, 6061–6072, doi:10.1029/JA075i031p06061.

Onsager, T. G., C. A. Kletzing, J. B. Austin, and H. MacKiernan (1993), Model of magnetosheath plasma in the magnetosphere: Cusp and mantle particles at low-latitudes, *Geophys. Res. Lett.*, *20*, 479–482, doi:10.1029/93GL00596.

Pilipp, W. G., and G. Morfill (1978), The formation of the plasma sheet resulting from plasma mantle dynamics, *J. Geophys. Res.*, *83*, 5670–5678, doi:10.1029/JA083iA12p05670.

Poppe, A. R., R. Samad, J. S. Halekas, M. Sarantos, G. T. Delory, W. M. Farrell, V. Angelopoulos, and J. P. McFadden (2012), ARTEMIS observations of lunar pick-up ions in the terrestrial magnetotail lobes, *Geophys. Res. Lett.*, *39*, L17104, doi:10.1029/2012GL052909.

Powell, K. G., P. L. Roe, T. J. Linde, T. I. Gombosi, and D. L. de Zeeuw (1999), A solution-adaptive upwind scheme for ideal magnetohydrodynamics, *J. Comput. Phys.*, *154*, 284–309, doi:10.1006/jcph.1999.6299.

Richard, R. L., L. M. Zelenyi, and M. Ashour-Abdalla (1995), Modeling the linear transient response of the magnetotail to variations in the plasma mantle, *J. Geophys. Res.*, *100*, 21,835–21,841, doi:10.1029/95JA02388.

Ridley, A. J., T. I. Gombosi, and D. L. DeZeeuw (2004), Ionospheric control of the magnetosphere: Conductance, *Ann. Geophys.*, *22*, 567–584, doi:10.5194/angeo-22-567-2004.

Rosenbauer, H., H. Grünwaldt, M. D. Montgomery, G. Paschmann, and N. Sckopke (1975), Heos 2 plasma observations in the distant polar magnetosphere: The plasma mantle, *J. Geophys. Res.*, *80*, 2723–2737, doi:10.1029/JA080i019p02723.

Seki, K., M. Hirahara, T. Terasawa, T. Mukai, Y. Saito, S. Machida, T. Yamamoto, and S. Kokubun (1998), Statistical properties and possible supply mechanisms of tailward cold O^+ beams in the lobe/mantle regions, *J. Geophys. Res.*, *103*, 4477–4489, doi:10.1029/97JA02137.

Sibeck, D. G., and R.-Q. Lin (2014), Size and shape of the distant magnetotail, *J. Geophys Res. Space Physics*, *119*, 1028–1043, doi:10.1002/2013JA019471.

Sibeck, D. G., et al. (2011), ARTEMIS science objectives, *Space Sci. Rev.*, *165*, 59–91, doi:10.1007/s11214-011-9777-9.

Siscoe, G., and Z. Kaymaz (1999), Spatial relations of mantle and plasma sheet, *J. Geophys. Res.*, *104*, 14,639–14,646, doi:10.1029/1999JA900113.

Siscoe, G. L., and E. Sanchez (1987), An MHD model for the complete open magnetotail boundary, *J. Geophys. Res.*, *92*, 7405–7412, doi:10.1029/JA092iA07p07405.

Siscoe, G. L., L. A. Frank, K. L. Ackerson, and W. R. Paterson (1994), Properties of mantle-like magnetotail boundary layer: Geotail data compared with a mantle model, *Geophys. Res. Lett.*, *21*, 2975–2978, doi:10.1029/94GL01601.

Siscoe, G. L., G. M. Erickson, B. U. Sonnerup, N. C. Maynard, K. D. Siebert, D. R. Weimer, and W. W. White (2001), Relation between cusp and mantle in MHD simulation, *J. Geophys. Res.*, *106*, 10,743–10,749, doi:10.1029/2000JA000385.

Stepanova, M., V. Pinto, J. A. Valdivia, and E. E. Antonova (2011), Spatial distribution of the eddy diffusion coefficients in the plasma sheet during quiet time and substorms from THEMIS satellite data, *J. Geophys. Res.*, *116*, A00I24, doi:10.1029/2010JA015887.

Taguchi, S., H. Kishida, T. Mukai, and Y. Saito (2001), Low-latitude plasma mantle in the near-Earth magnetosphere: Geotail observations, *J. Geophys. Res.*, *106*, 1949–1954, doi:10.1029/2000JA900100.

Tóth, G., et al. (2012), Adaptive numerical algorithms in space weather modeling, *J. Comput. Phys.*, *231*, 870–903, doi:10.1016/j.jcp.2011.02.006.

Wang, C.-P., L. R. Lyons, T. Nagai, J. M. Weygand, and A. T. Y. Lui (2010), Evolution of plasma sheet particle content under different interplanetary magnetic field conditions, *J. Geophys. Res.*, *115*, A06210, doi:10.1029/2009JA015028.

Wang, J. Y., C. Wang, Z. H. Huang, and T. R. Sun (2014), Effects of the interplanetary magnetic field on the twisting of the magnetotail: Global MHD results, *J. Geophys. Res. Space Physics*, *119*, 1887–1897, doi:10.1002/2013JA019257.